Journal of Materials Chemistry A

COMMUNICATION

View Article Online
View Journal | View Issue

Cite this: J. Mater. Chem. A, 2017, 5, 23471

Received 28th September 2017
Accepted 1st November 2017

DOI: 10.1039/c7ta08597d

rsc.li/materials-a

Ultrathin molybdenum boride films for highly efficient catalysis of the hydrogen evolution reaction†

Xufeng Wang,[ab] Guoan Tai,*[ab] Zenghui Wu,[ab] Tingsong Hu[ab] and Rui Wang[ab]

All molybdenum borides with various phases such as Mo_2B, α-MoB, β-MoB, and MoB_2 have been found to possess excellent electrocatalytic hydrogen evolution reaction (HER) activity. Ultrathin two-dimensional (2D) borides are expected to have both maximized surface active sites and fast electron transport, ensuring higher HER activity. Here we report the large-area preparation of ultrathin hexagonal Mo_3B films of 6.48 nm thickness on Mo foils by chemical vapour deposition using a mixture of boron and boron oxide powders as the boron source, and hydrogen gas as both the carrier and reducing gas. The ultrathin film exhibits fantastic stability in acidic solution and has a small Tafel slope of 52 mV dec^{-1} which is the lowest value so far reported for molybdenum boride catalysts. Furthermore, our first-principles calculations show that the ultrathin Mo_3B film is metallic, which facilitates fast electron transport along the active edges of the thin film for enhancing the HER activity.

Boron-based materials have drawn significant attention because of their remarkable physical and chemical properties, such as inconceivable structural complexity, high mechanical strength, superconductivity, thermoelectricity, excellent chemical stability and high catalytic performance.[1–4] They should find extensive applications in highly efficient catalysis, thermal neutron detectors, flat plane displays and electron emission nanodevices. For elemental boron, its electron deficiency gives rise to abundant allotropes in the bulk, suggesting diverse fascinating chemistries with unusual structures and multi-center bonding.[5–8] However, boron cannot form hexagonal monolayers like graphene because of its electron deficiency.[9] Theoretical studies suggested that buckled triangular boron lattice sheets with partially filled hexagonal holes are stable.[5,10–12] Boron monolayers with diverse hole structures and densities have been predicted on suitable substrates such as Cu (111) and Ag (111).[13–15] Experimentally, our group reported the formation of γ-B_{28} two-dimensional (2D) films on a copper surface, consisting of B_{12} cages intercalated by B_2 units.[16] After that, borophenes have been synthesized on silver surfaces using molecular beam epitaxy techniques.[17,18] The research advances pave the way for potential applications of boron monolayers in nanoscale electrical devices, and highly efficient energy conversion and storage.

Following the discovery of boron monolayers, 2D metal borides with covalent networks have also attracted enormous interest owing to their unique structural, electronic, mechanical, optical, thermal and magnetic properties.[19–22] Among these borides, theoretical predictions suggested that molybdenum borides have abundant structures to represent fascinating mechanical and chemical properties, which is established by the arrangement and proportion of boron and molybdenum atoms in a unit cell.[23,24] In sharp contrast to molybdenum sulphides,[25–27] molybdenum borides have peculiar crystal structures, which make the activity of these catalysts not easily explained by the presence of unsaturated edge sites.[4,28,29] They have both good conductivity and abundant catalytically active sites arising from the serious electron deficiency of boron atoms, which will lead to highly efficient electrocatalytic hydrogen evolution reaction (HER) activity. Hu *et al.* found that the commercial polycrystalline MoB powders exhibited excellent electrocatalytic activities under both acidic and alkaline conditions.[4] Recently, Fokwa's team synthesized four binary bulk molybdenum borides Mo_2B, α-MoB, β-MoB, and MoB_2 by arc-melting approaches, and found that the HER activity of the borides increases with increasing boron content.[28] Besides, ultrathin 2D materials possess maximized surface electroactive sites resulting in the decrease of the diffusion length of ions and increase of the contact area with the electrolyte.[30,31] Moreover, the reported metal borides are usually metallic, implying that the materials are significantly conductive. Therefore, fast

[a]The State Key Laboratory of Mechanics and Control of Mechanical Structures, Laboratory of Intelligent Nano Materials and Devices of Ministry of Education, College of Aerospace Engineering, Nanjing University of Aeronautics and Astronautics, Nanjing 210016, China. E-mail: taiguoan@nuaa.edu.cn

[b]School of Material Science and Technology, Nanjing University of Aeronautics and Astronautics, Nanjing 210016, China

† Electronic supplementary information (ESI) available. See DOI: 10.1039/c7ta08597d

electron transport and abundant catalytically active edges guarantee that 2D metal borides should have higher electrocatalytic HER activity than the corresponding bulk. Until now, however, 2D molybdenum boride films have not been realized in experiments, let alone studied for their catalytic properties.

Herein, we report the large-area preparation of ultrathin Mo_3B films with a thickness of 6.48 nm on Mo foils by chemical vapour deposition, where Mo foil was selected as the Mo source, a mixture of high-purity boron and boron oxide powders as the boron source, and hydrogen (H_2) gas as both the carrier and reducing gas. The structure of the ultrathin films was characterized by high resolution transmission electron microscopy, selected area electron diffraction and energy dispersive spectroscopy. Our first-principles calculations reveal that the Mo_3B film is metallic, which allows for fast electron transport along the active edges for potential application in the highly efficient electrocatalytic HER. The measured results show that the thin films exhibit extremely excellent catalytic performance with fantastic cycling stability and striking resistance to corrosion.

We prepared the ultrathin Mo_3B films *via* a home-made two-zone CVD furnace, and the schematic diagram of the growth set-up is shown in Fig. S1 (ESI†). The temperature of the two-zone furnace is separately controlled for the source zone (T_1) and the deposition zone (T_2). Before the growth, to ensure the formation of a smooth foil surface and enlarge the grain boundaries, the Mo foils were annealed at 1400 °C for 10 h in a 50 sccm H_2 gas (Fig. 1a (below) and Fig. S2, ESI†).[32] Consequently, the mixture of boron (B) and boron oxide (B_2O_3) powders in the T_1 zone was annealed at 1100 °C to produce the diboron dioxide (B_2O_2) vapour, and the ultrathin films were controllably prepared in the T_2 zone at 900 °C for 1 h in a 10 sccm H_2 atmosphere (Fig. 1a). After the growth, the surface of the thin films on the Mo foil became slightly rough, as shown in Fig. 1a (top). Finally, the films were transferred onto various substrates for further characterization (see the Methods section).

The crystal structure of the Mo_3B ultrathin films is displayed in Fig. 1b–d. It features a hexagonal (rhombohedral) symmetry with a space group of $P6_3/mmc$ ($R\bar{3}m$). The top view of the crystal structure in the *ab* projection shows that the structure is hexagonal, in which boron and Mo atoms are located at 2*c* and 2*b* (4-f) sites, respectively (Fig. 1b). A unit cell of 14 atoms (a = 4.568, b = 4.568, c = 7.150 Å) is displayed in the *ac* projection (Fig. 1c). The stoichiometric ratio of Mo and B is verified as 3 : 1. The side view of the structure in the *bc* projection suggests the appearance of substantially exposed Mo and B sites on the surface of the thin film (Fig. 1d), which offer proficient catalytically active sites for improving the catalytic activity of the thin film toward the highly efficient HER.

An ultrathin Mo_3B film was transferred to a 285 nm SiO_2/Si substrate by wiping off the bottom Mo foil with 2 M $FeCl_3$ solution. The corresponding optical image shows that the film has a large area and is ultrathin (Fig. 2a). Furthermore, scanning electron microscopy (SEM) was utilized to characterize the morphology of the Mo_3B films (Fig. S2a, b and S3a, ESI†). The results show that the ultrathin Mo_3B film is grown on the surface of the Mo foil, which is completely different from annealing the Mo foil (Fig. S2c and d, ESI†). Furthermore, we obtained the energy dispersive X-ray (EDX) spectrum of the rectangular area shown in the SEM image of the Mo_3B film on the SiO_2/Si substrate (Fig. S3b, ESI†). The EDX spectrum unambiguously verified that the Mo and B ratio is approx. 3 : 1, in good agreement with the predicted ratio of Mo_3B. The corresponding EDS mapping analysis reveals a homogeneous distribution of Mo and B elements in the sample, as shown in

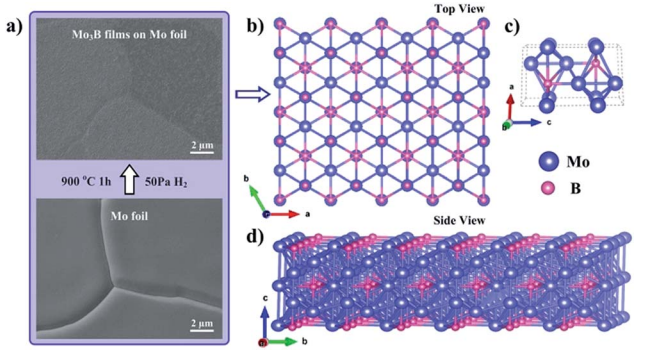

Fig. 1 Scanning electron microscopy (SEM) image and crystal structure of ultrathin Mo_3B films. (a) SEM images of the Mo foil (below) and ultrathin Mo_3B films on the Mo foil (top). (b) Top view of the ultrathin Mo_3B film. (c) Structure of the basic unit cell of the thin film shown in the *ac* projection. (d) Side view of the ultrathin Mo_3B film. Unit cell vectors are shown in (b–d).

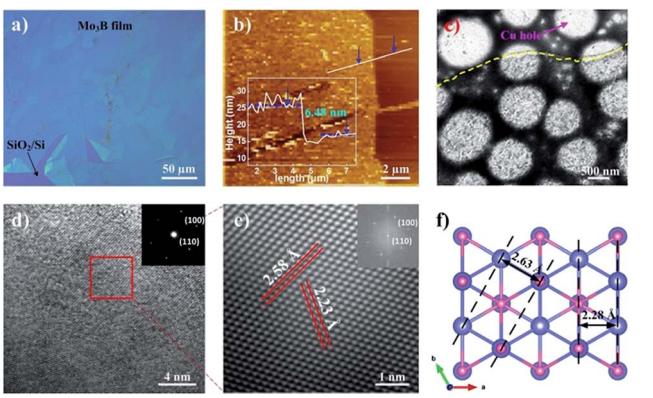

Fig. 2 Structural characterization of the ultrathin Mo_3B films. (a) Optical image of the Mo_3B ultrathin film on a 285 nm SiO_2/Si substrate. (b) AFM image of the ultrathin film transferred to the substrate. The height profile along the white line shows a thickness of 6.48 nm at the bottom left corner of the inset, indicating that the film is ultrathin. (c) Low-magnification TEM image of the ultrathin film transferred to the holes of a Cu net without the carbon film. The yellow dotted line represents the edge of the thin film. The pink arrow refers to the hole of the Cu net. (d) High-magnification TEM image of the ultrathin film. The inset at the upper right is the SAED image. (e) High-resolution TEM image taken from the area shown by the red box in (d). The inset is the corresponding fast Fourier transform (FFT) pattern, indicating that the crystal structure is hexagonal. The lattice spacings of 2.23 and 2.58 Å can be respectively indexed to the (100) and (110) crystal faces of hexagonal Mo_3B. (f) Structure of the hexagonal Mo_3B thin film. The two oppositely charged sublattices are indicated in different colours (Mo: royalblue; B: magenta).

Fig. S3c and d (ESI†). Moreover, the grazing angle incidence X-ray diffraction (XRD) pattern of the ultrathin film on the Mo foil demonstrates that a characteristic diffraction peak can be indexed to the (110) lattice plane of the Mo_3B crystal, which is in good agreement with the XRD pattern predicted by using the JEMS electron microscopy simulation software (Fig. S4, ESI†). To further evaluate the thickness of the ultrathin film, the atomic force microscopy (AFM) image was obtained and it shows that the thickness of the Mo_3B film is 6.48 nm (Fig. 2b), which fits well with those of widely accepted ultrathin films.[33]

Transmission electron microscopy (TEM) and the corresponding selected-area electron diffraction (SAED) were adopted to confirm the quality and lattice structure of the Mo_3B films. The low magnification TEM image shows that the film is ultrathin and has a large area (Fig. 2c). The high resolution TEM (HRTEM) image and the corresponding SAED pattern show that the ultrathin film exhibits high crystallinity (Fig. 2d). The corresponding atomic layer of the thin film was reconstructed by masking the two-dimensional fast Fourier transform (FFT) pattern (the inset of Fig. 2e), and the result reveals that the thin film has a hexagonal lattice structure with lattice spacings of approximately 2.23 and 2.58 Å, which correspond to the (100) and (110) crystal planes of the rhombohedral Mo_3B, respectively. The experimental results are excellent and consistent with the structural parameters obtained by first-principles calculations (Fig. 2f).

To gain insight into the electronic properties of the ultrathin Mo_3B film, first-principles calculations within the density functional theory framework, based on the Cambridge Sequential Total Energy Package known as CASTEP, were performed to determine the exchange–correlation potential of the Mo_3B. The in-plane electronic structure and electronic states of the sample along the *c*-axis were illustrated by the dispersions along the high-symmetry points (*K*, *Z*, *G*, *F*, *H*, *Q* and *Z*), as shown in Fig. 3a. It was found that the top of the valence band goes through the bottom of the conduction band, denoting that the Mo_3B thin film is metallic. Our calculated projected electronic density of states (PDOS) to understand the bonding mechanism of Mo_3B is plotted in Fig. 3b. The major orbital occupancy near the Fermi level can be attributed to Mo 4d orbital electrons which are the principal cause of the metallicity. The charge density of the Mo_3B thin film shows that the electron densities around Mo decrease while an enhancement of the electron density is observed at each B atom (Fig. 3c). This structure allows the charge-transfer from Mo to B atoms, which reduces the d-band center of Mo atoms and further decreases the hydrogen-binding energy. The result, in turn, favors the electrochemical desorption of H_{ads} and results in a relatively moderate Mo–H binding strength, which brings about the enhancement of the electrochemical HER activity. By calculating the free energy of adsorbed H on the surface of the Mo_3B thin film based on the Sabatier principle (Fig. 3d and S5, ESI†), free energies of ultrathin Mo_3B film surfaces terminated with Mo–B and Mo are respectively −0.22 and −0.30 eV while they are remarkably closer to the Fermi level compared with −0.56 eV of the Mo foil, suggesting that the ultrathin Mo_3B film with high exposure of boron atoms should have excellent

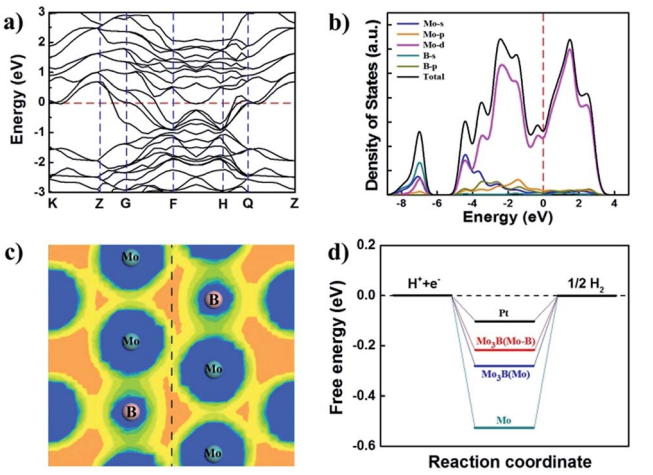

Fig. 3 First-principles calculations of the electronic properties of the Mo_3B thin film. (a) The electronic band structure of the Mo_3B thin film. The Fermi level is shown by the red dashed line. (b) Calculated total density of states (black line) and the local density of states of the Mo (s, p and d) and B (s and p). (c) Electron density map of the ultrathin Mo_3B film. (d) Free energy evolution of H with respect to the standard hydrogen electrode (SHE) during the HER catalysed by various materials.

catalytic performance compared to pure Mo metal. Therefore, combining the excellent electrical conductivity and a large amount of active edge sites facilitates highly efficient catalytic activity in the HER.

The density of states (DOS) of Mo_3B surfaces with Mo–B and Mo terminations and Mo_3B nanosheets has also been calculated to demonstrate the significance of synthesizing the ultrathin 2D structure, as shown in Fig. S6 (ESI†). It can be observed that the d-band center energies of Mo_3B surfaces terminated with Mo–B and Mo are −2.10 and −2.15 eV, respectively. The downshift of the d-band center of the Mo_3B surface terminated with Mo–B leads to the decrease of the hydrogen binding energy (HBE) which enhances the HER activity owing to higher exposure of Mo and B atoms on the Mo_3B (001) surface.[34,35] Furthermore, decreasing the thickness of the nanofilms will improve the HER activity again.[36]

To probe the purity and electronic structure of the ultrathin Mo_3B film, Mo 3d and B 1s core level XPS spectra were respectively measured (Fig. S7, ESI†). The peaks located at 231.4 and 228.2 eV in the Mo 3d spectrum can be attributed to the borides (Fig. S7a, ESI†).[4,28] To discuss the oxidation state of Mo element in the film, the deconvolution of the spectrum which indicates two doublets at 236.1/232.9 eV (Mo^{6+} $3d_{3/2}/3d_{5/2}$) and 231.7/228.8 eV (Mo^{4+} $3d_{3/2}/3d_{5/2}$) which can be assigned to the high oxidation state of Mo (MoO_3 and MoO_2).[4,28] The B 1s spectrum of the ultrathin Mo_3B film was also deconvoluted into two distinct species at 189.3 and 193.3 eV (Fig. S7b, ESI†). The former is assigned to the interaction of boron with molybdenum while the latter is due to boron-oxo species.[28]

The electrocatalytic HER activity of the ultrathin Mo_3B films for the water splitting reaction was measured in 0.5 M H_2SO_4 using a standard three-electrode system. During this activation

process, a calomel electrode and a high-purity graphite rod were adopted as the reference and the counter electrode, respectively. To compensate for the voltage drop between the working and the reference electrode, an *iR* correction was realized in the polarization process, and the obtained *iR*-corrected polarization curves of the samples are shown in Fig. 4a. Bare Mo foil and commercial Pt foil were also tested for comparison. The ultrathin Mo_3B film on the Mo foil synthesized at 900 °C for 1 h exhibits a remarkably high electrocatalytic activity with an onset potential of 115 mV. The overpotential of the Mo_3B film is 249 mV at a constant current density of 20 mA cm^{-2} which is considered as a typical reference metric for the electrocatalytic performance.[31] In comparison, the films grown at 700, 800 and 1000 °C for 1 h have overpotentials of 334, 305 and 391 mV, respectively. The performance degradation results from the formation of amorphous structures at 700, 800 and 1000 °C which weakens the electron transport along the surface of the thin films (Fig. S8, ESI†). The oxidation of the Mo surface cannot be used to explain the high electrocatalytic activity of the ultrathin Mo_3B film (Fig. S9, ESI†), suggesting that exposed boron atoms should be responsible for the high HER activity.

To understand the underlying mechanism of the highly efficient electrochemical HER activity, Tafel slopes derived from the polarization curves are obtained, as shown in Fig. 4b. The linear segments of the plots were fitted to the Tafel equation ($\eta = b\log(j) + a$, where j is the current density and b is the Tafel slope). In agreement with the reported value,[31,37] the measured Tafel slope of the Pt foil is 30 mV per decade. The ultrathin Mo_3B film grown at 900 °C for 1 h has a small Tafel slope down to 52 mV per decade, while the films synthesized at 700, 800 and 1000 °C for 1 h give rise to Tafel slopes up to 64, 72 and 94 mV per decade, respectively. Besides, the bare Mo foil achieves a Tafel slope of 146 mV per decade. It is noted that the small Tafel slope is preferable for practical catalytic application because it is responsible for a high HER rate at the same overpotential.[35] The small overpotential and Tafel slope of the ultrathin Mo_3B film exhibit unique superiorities in a highly efficient HER in comparison with other molybdenum-based materials, as shown in Fig. S10 and Table S1 (ESI†). The experimental results further reveal that the ultrathin Mo_3B film synthesized at 900 °C for 1 h has an excellent HER activity. Furthermore, the electrochemical double-layer capacitance (C_{dl}) was measured to evaluate the electrochemically active areas. The ultrathin Mo_3B film grown at 900 °C exhibits a C_{dl} of 16.62 mF cm^{-2} which is larger than those of the nanofilms obtained at 700, 800 and 1000 °C (Fig. S11, ESI†).

The interfacial properties and HER kinetics of the ultrathin Mo_3B films on Mo foil could be analyzed by electrochemical impedance spectroscopy (EIS). Equivalent circuit models based on an electrochemical reaction as the circuit elements were utilized to investigate the electrode/electrolyte interface and comprehend the physical meaning of action processes.[38] The Nyquist plots of the films were measured in a frequency range of 10^{-2} to 10^{5} Hz under a 5 mV AC signal amplitude (Fig. 4c), and the equivalent circuit model is shown in the top right corner of Fig. 4c. The resistance of the electrolyte (R_s, namely, R_1 in the model) and charge-transfer resistance (R_{ct}, namely, R_2 in the model) as well as CPE associated with the kinetics of the HER of each film and bare Mo foil are shown in Table S2.† The ultrathin Mo_3B films exhibit much lower R_{ct} than the bare Mo foil and other thin films on the Mo foils. The results further demonstrate that the crystallinity of the films favors charge transport on the electrode/electrolyte interface to enhance the electrocatalytic performance.

To assess the durability of the ultrathin Mo_3B films during electrocatalytic hydrogen evolution progress in acidic solution, we performed cyclic voltammetry (CV) sweeps varying from 0 to −0.6 V (*vs.* the RHE) at a scan rate of 50 mV s^{-1}. After 2500 CV sweeps, a negligible degradation of cathodic current was observed, and the overpotentials at current densities of 20 and 60 mA cm^{-2} increased by less than 10 and 15 mV, respectively (Fig. 4d). The stability was also elucidated using a constant overpotential of 0.2 V during a long period of 15 h, and there was no significant current degradation, suggesting that the ultrathin Mo_3B film was extremely stable under HER conditions, as shown in Fig. S12.† Furthermore, the crystal structure stability was determined from the HRTEM images, which indicated that the sample still retained the hexagonal structure after 1000 and 3000 CV sweeps despite the slight structural distortion of the sample (Fig. S13†).

In conclusion, ultrathin crystalline Mo_3B films have been successfully synthesized on molybdenum foils by chemical vapor deposition. Because of not only exposed Mo and B sites providing abundant active sites, but also crystalline and metallic structure characters giving rise to excellent electrical conductivity, the ultrathin Mo_3B films exhibit striking catalytic performance, superlong cycling stability and significant resistance to corrosion. Our work has opened the door for future

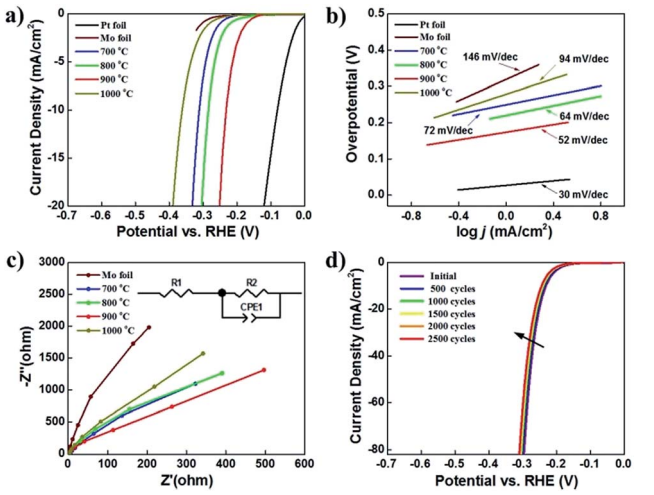

Fig. 4 Electrocatalytic performance of ultrathin Mo_3B films. (a) HER *iR*-corrected LSV curves of ultrathin Mo_3B films on the Mo foil in 0.5 M H_2SO_4, along with a pure Mo foil and a standard Pt electrode. The scan rate is 5 mV s^{-1}. (b) Corresponding Tafel plots (log current *versus* potential) of the samples in comparison with that of the Pt foil. (c) Electrochemical impedance spectroscopy (EIS) Nyquist plots of the samples grown at different temperatures. (d) Stability tests of the Mo_3B film grown at 900 °C for 1 h through potential cycling. Violet line: the polarization curve of the sample at the initial time. Red line: the polarization curve of the sample after 2500 cycles.

studies and potential applications of molybdenum boride with diverse phase structures and other 2D metal borides in advanced HER electrocatalysis.

Conflicts of interest

There are no conflicts of interest to declare.

Acknowledgements

This work was supported by the NSF (61474063 and 61774085), Jiangsu NSF (BK20151475), Six talent peaks project in Jiangsu Province (XCL-046), the Fundamental Research Funds for the Central Universities (NE2017101), the Foundation of Graduate Innovation Center in NUAA (kfjj20170605) and the Priority Academic Program Development of Jiangsu Higher Education Institutions. We thank Dr C. Li for his theoretical help.

Notes and references

1 G. Akopov, M. T. Yeung and R. B. Kaner, *Adv. Mater.*, 2017, **29**, 1604506.
2 B. Albert and H. Hillebrecht, *Angew. Chem., Int. Ed.*, 2009, **48**, 8640–8668; *Angew. Chem.*, 2009, **121**, 8794–8824.
3 A. P. Sergeeva, I. A. Popov, Z. A. Piazza, W. L. Li, C. Romanescu, L. S. Wang and A. I. Boldyrev, *Acc. Chem. Res.*, 2014, **47**, 1349–1358.
4 H. Vrubel and X. L. Hu, *Angew. Chem., Int. Ed.*, 2012, **51**, 12703–12706; *Angew. Chem.*, 2012, **124**, 12875–12878.
5 E. S. Penev, S. Bhowmick, A. Sadrzadeh and B. I. Yakobson, *Nano Lett.*, 2012, **12**, 2441–2445.
6 A. R. Oganov, J. H. Chen, C. Gatti, Y. Z. Ma, Y. M. Ma, C. W. Glass, Z. X. Liu, T. Yu, O. O. Kurakevych and V. L. Solozhenko, *Nature*, 2009, **457**, 863–867.
7 H. J. Zhai, Y. F. Zhao, W. L. Li, Q. Chen, H. Bai, H. S. Hu, Z. A. Piazza, W. J. Tian, H. G. Lu, Y. B. Wu, Y. W. Mu, G. F. Wei, Z. P. Liu, J. Li, S. D. Li and L. S. Wang, *Nat. Chem.*, 2014, **6**, 727–731.
8 M. A. White, A. B. Cerqueira, C. A. Whitman, M. B. Johnson and T. Ogitsu, *Angew. Chem., Int. Ed.*, 2015, **54**, 3626–3629; *Angew. Chem.*, 2015, **127**, 3697–3700.
9 Z. Zhang, E. S. Penev and B. I. Yakobson, *Nat. Chem.*, 2016, **8**, 525–527.
10 M. C. Hersam, *ACS Nano*, 2015, **9**, 4661–4663.
11 X. J. Wu, J. Dai, Y. Zhao, Z. W. Zhuo, J. L. Yang and X. C. Zeng, *ACS Nano*, 2012, **6**, 7443–7453.
12 I. Boustani, *Surf. Sci.*, 1997, **370**, 355–363.
13 Z. H. Zhang, Y. Yang, G. Y. Gao and B. I. Yakobson, *Angew. Chem., Int. Ed.*, 2015, **54**, 13022–13026; *Angew. Chem.*, 2015, **127**, 13214–13218.
14 Y. Y. Liu, E. S. Penev and B. I. Yakobson, *Angew. Chem., Int. Ed.*, 2013, **52**, 3156–3159; *Angew. Chem.*, 2013, **125**, 3238–3241.
15 H. S. Liu, J. F. Gao and J. J. Zhao, *Sci. Rep.*, 2013, **3**, 3238.
16 G. Tai, Y. G. Zhou, X. F. Wang, J. Z. Kong, T. Zeng, Y. C. You and Q. Wang, *Angew. Chem., Int. Ed.*, 2015, **54**, 15473–15477; *Angew. Chem.*, 2015, **127**, 15693–15697.
17 A. J. Mannix, X. F. Zhou, B. Kiraly, J. D. Wood, D. Alducin, B. D. Myers, X. L. Liu, B. L. Fisher, U. Santiago, J. R. Guest, M. J. Yacaman, A. Ponce, A. R. Oganov, M. C. Hersam and N. P. Guisinger, *Science*, 2015, **350**, 1513–1516.
18 B. Feng, J. Zhang, Q. Zhong, W. Li, S. Li, H. Li, P. Cheng, S. Meng, L. Chen and K. Wu, *Nat. Chem.*, 2016, **8**, 563–568.
19 W. L. Li, T. Jian, X. Chen, T. T. Chen, G. V. Lopez, J. Li and L. S. Wang, *Angew. Chem., Int. Ed.*, 2016, **55**, 7358–7363; *Angew. Chem.*, 2016, **128**, 7484–7489.
20 H. Zhang, Y. Li, J. Hou, K. Tu and Z. Chen, *J. Am. Chem. Soc.*, 2016, **138**, 5644–5651.
21 S. K. Das, A. Bedar, A. Kannan and K. Jasuja, *Sci. Rep.*, 2015, **5**, 10522.
22 L. Z. Zhang, Z. F. Wang, S. X. Du, H. J. Gao and F. Liu, *Phys. Rev. B*, 2014, **90**, 161402(R).
23 R. F. Zhang, D. Legut, Z. J. Lin, Y. S. Zhao, H. K. Mao and S. Veprek, *Phys. Rev. Lett.*, 2012, **108**, 255502.
24 A. T. Lech, C. L. Turner, R. Mohammadi, S. H. Tolbert and R. B. Kaner, *Proc. Natl. Acad. Sci. U. S. A.*, 2015, **112**, 3223–3228.
25 T. F. Jaramillo, K. P. Jorgensen, J. Bonde, J. H. Nielsen, S. Horch and I. Chorkendorff, *Science*, 2007, **317**, 100–102.
26 J. Kibsgaard, T. F. Jaramillo and F. Besenbacher, *Nat. Chem.*, 2014, **6**, 248–253.
27 J. Kibsgaard, Z. B. Chen, B. N. Reinecke and T. F. Jaramillo, *Nat. Mater.*, 2012, **11**, 963–969.
28 H. Park, A. Encinas, J. P. Scheifers, Y. Zhang and B. P. T. Fokwa, *Angew. Chem., Int. Ed.*, 2017, **56**, 5575–5578; *Angew. Chem.*, 2017, **129**, 5667–5670.
29 S. Carenco, D. Portehault, C. Boissiere, N. Mezailles and C. Sanchez, *Chem. Rev.*, 2013, **113**, 7981–8065.
30 D. Voiry, J. Yang and M. Chhowalla, *Adv. Mater.*, 2016, **28**, 6197–6206.
31 T. S. Hu, K. Bian, G. Tai, T. Zeng, X. F. Wang, X. H. Huang, K. Xiong and K. J. Zhu, *J. Phys. Chem. C*, 2016, **120**, 25843–25850.
32 G. Tai, T. Zeng, J. HuYu, J. Zhou, Y. You, X. Wang, H. Wu, X. Sun, T. Hu and W. Guo, *Nanoscale*, 2016, **8**, 2234–2241.
33 C. Tan, X. Cao, X. J. Wu, Q. He, J. Yang, X. Zhang, J. Chen, W. Zhao, S. Han, G. H. Nam, M. Sindoro and H. Zhang, *Chem. Rev.*, 2017, **117**, 6225–6331.
34 W.-F. Chen, K. Sasaki, C. Ma, A. I. Frenkel, N. Marinkovic, J. T. Muckerman, Y. Zhu and R. R. Adzic, *Angew. Chem., Int. Ed.*, 2012, **51**, 6131–6135; *Angew. Chem.*, 2012, **124**, 6235–6239.
35 C. G. Morales-Guio, L.-A. Stern and X. L. Hu, *Chem. Soc. Rev.*, 2014, **43**, 6555–6559.
36 J. H. Huang, J. T. Chen, T. Yao, J. F. He, S. Liang, Z. H. Sun, Q. H. Liu, W. R. Cheng, F. C. Hu, Y. Jiang, Z. Y. Pan and S. Q. Wei, *Angew. Chem., Int. Ed.*, 2015, **54**, 8722–8727; *Angew. Chem.*, 2015, **127**, 8846–8851.
37 Y. Li, H. Wang, L. Xie, Y. Liang, G. Hong and H. Dai, *J. Am. Chem. Soc.*, 2011, **133**, 7296–7299.
38 Y. Tan, P. Liu, L. Chen, W. Cong, Y. Ito, J. Han, X. Guo, Z. Tang, T. Fujita, A. Hirata and M. W. Chen, *Adv. Mater.*, 2014, **26**, 8023–8028.